

Evaluating ice fabrics using fabric analyser techniques in Sørtdal Glacier, East Antarctica

Christopher J.L. WILSON,¹ Mark PETERNELL²

¹*School of Geosciences, Monash University, Victoria 3800, Australia
E-mail: Chris.Wilson@monash.edu*

²*Department of Earth Sciences, University of Mainz, D-55099 Mainz, Germany*

ABSTRACT. Ice cores (~4 m long) obtained from areas of different surface velocities near the terminus of Sørtdal Glacier, East Antarctica, have been investigated using two versions of a fabric analyser (G50). In sections parallel to the flow plane, the microstructure is typically interlocking with elongate grains that parallel air-bubble elongation, X , reflecting their development in an earlier ductile regime. The c -axis fabric patterns vary with respect to X and vary from single–double maxima to asymmetric small-circle girdles oblique to the planar foliation, which can be attributed to a simple shear regime. The site-to-site variations in the c -axis patterns can be related to areas of different surface velocities, the asymmetry of fabrics correlating with localized strain variations and differences in the deformation path, but not to the current strain pattern recorded by the near-surface deformation conditions. Overprinting fractures have little effect on microstructure except for local dissolution and precipitation along stylolitic surfaces. Comparison of results from the two different fabric analysers reveals that with a higher pixel resolution the incorporation of additional monochromatic light-emitting diodes and repositioning of a retarder plate produce more reliable c -axis measurements.

INTRODUCTION

In general, deformation in a glacier tends to localize into narrow zones and is governed by the deformation of the polycrystalline ice as the ice interacts with its bedrock. The driving force for the internal deformation is shear stress induced by gravitational forces acting on the sloping ice body. Deformation in such high-strain zones is usually non-coaxial (i.e. the principal axes of finite strain do not lie parallel to those of successive strain increments). This type of high-strain zone accommodates important differential displacements and is recognized in Sørtdal Glacier, East Antarctica (Patrick and others, 2003). Although the glaciological literature provides a lot of c -axis crystallographic fabric data, the interpretation of the more highly strained regions is ambiguous because it is very difficult to isolate the influence of each of the variables that contribute to the final pattern of the microfabric. The interpretation of fabric evolution in the upper levels of a glacier subject to high strain rates has advanced as new techniques for measuring microfibrils have been developed (e.g. Wilson and others, 2007a; Peternell and others, 2010) and our understanding of ice deformation in different environments has improved.

It is commonly thought that deformation mechanisms such as dislocation glide and diffusional flow (Petrenko and Whitworth, 1999) localize the deformation in zones that are softer than the surrounding material, i.e. when the stress needed to deform at a given strain rate is lower inside than outside the shear zone. Several physical processes may cause softening during deformation that could lead to strain localization in initially homogeneous materials (Poirier, 1980): geometrical softening (rotation of slip planes in more favourable orientations), microscale softening (e.g. dynamic recrystallization), strain softening (intracrystalline slip at a critical stress level) and strain-rate softening or thermal softening (e.g. shear heating). Other studies attribute softening to the development of a crystallographic preferred orientation in a grain-size sensitive regime of deformation

(superplastic) in fine-grained ice (Goldsby, 2009). Rather than producing strain themselves, these processes actually influence the strain-accommodating mechanisms and the strain-softening processes.

Strain softening has been observed in many large-strain deformation studies on ice (Wilson, 2000) and has typically been accompanied by changes in c -axis crystallographic preferred orientations and in grain size (Thorsteinsson and others, 1997). Contrary to what may be expected, strain localization, on a scale greater than the average grain size, is never observed in polycrystalline ice deformed in compression and has only been recorded in experiments where the superimposed boundary conditions force the strain to localize into specific zones (Wilson and Sim, 2002).

This study of the ice in Sørtdal Glacier was started with the following questions in mind. How far does Sørtdal Glacier provide information on the development of c -axis patterns in view of the differences in initial microstructure and strain distributions observed by Patrick and others (2003)? What information can be obtained from the fabrics about the deformation history? In order to answer these questions, the microstructure and crystallographic orientation patterns were analysed using two versions of a fabric analyser: the G50-white which is the most frequently used machine for analysing ice, and the G50-RGB, which is mainly used for petrological investigations but has been proven to be very accurate (Wilson and others, 2009; Peternell and others, 2010, 2011). There are several generations of G50-white machines, which can be separated into pre-2010 and post-2010 versions. All pre-2010 G50-white instruments have a lower resolution, whereas the post-2010 G50 has similar accuracy to the G50-RGB instrument. All instruments utilize the principles of the optical extinction in the optically uniaxial ice crystal between crossed polarizers (Wilén and others, 2003; Wilson and others, 2007a). For the comparison c -axes were measured from the same points inside individual ice grains and the aim is to

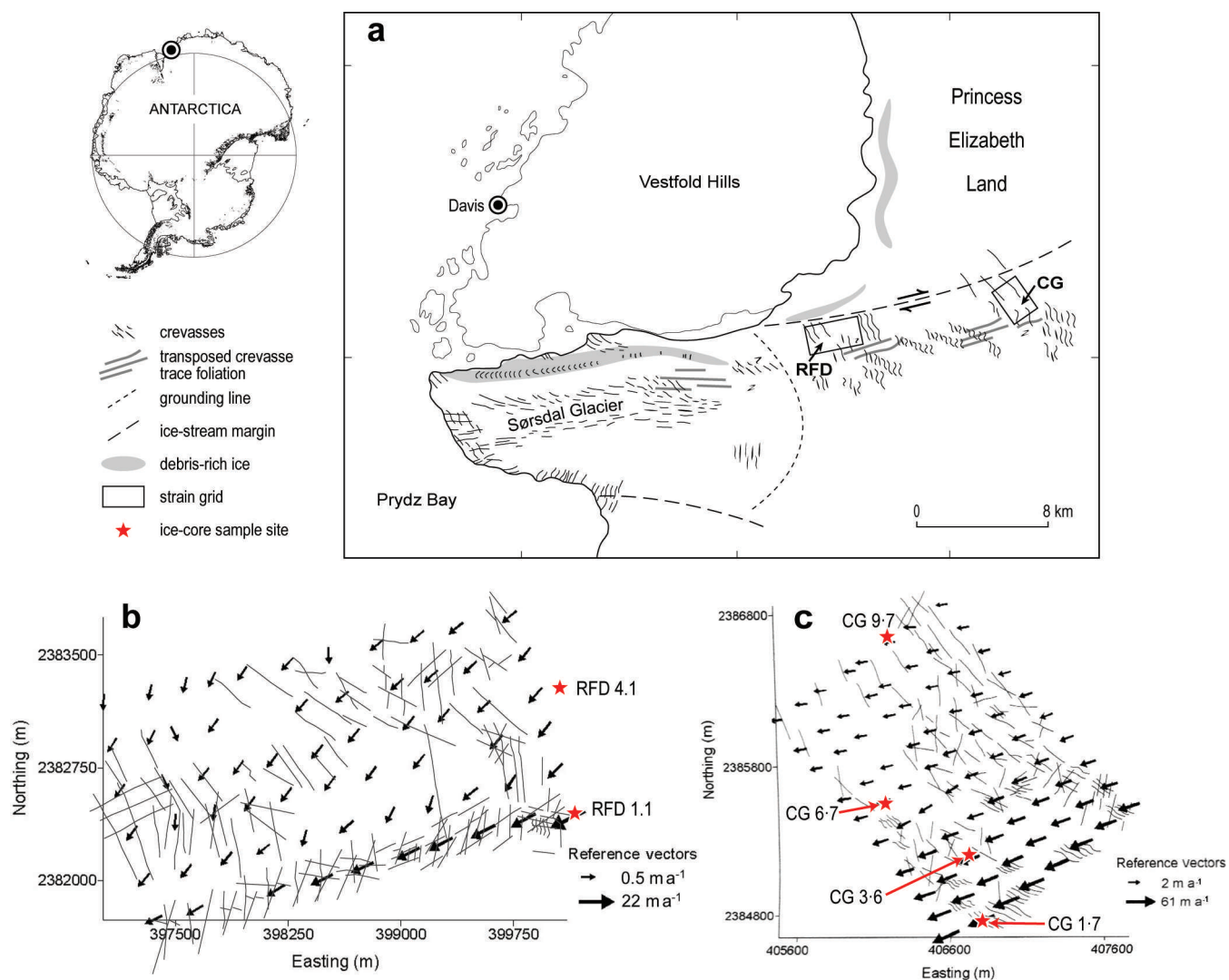


Fig. 1. Maps showing the location of the ice-coring sites in the Sørsdal Glacier–Vestfold Hills region. (a) The ice cores were obtained from the Russian Fuel Depot (RFD) site and the Christensen Grid (CG) area described by Patrick and others (2003). (b, c) Ice-core locations (star) superimposed on sketch of crevasse patterns and velocity vectors at the RFD (b) and CG (c) sites.

evaluate the accuracy of the pre-2010 G50-white and to compare the results with the G50-RGB instrument, which has been calibrated against electron backscatter diffraction (EBSD) results (Peternell and others, 2010).

STUDY AREA AND MICROFABRIC TECHNIQUES

This paper focuses on the microstructural aspects and *c*-axis crystallographic preferred orientations in samples taken from shallow ice cores in the terminus region of Sørsdal Glacier (Fig. 1). Sørsdal Glacier contains zones of anomalous high flow rates and localized strain, where the glacier surface records ice-flow velocities of $>114 \text{ m a}^{-1}$ (Patrick and others, 2003). Sørsdal Glacier is an east–west-flowing outlet glacier that is approximately 5–8 km wide and 120 km long and is the longest of a number of outlet ice streams from Princess Elizabeth and Wilhelm II Lands into Prydz Bay (Fig. 1a). It is located above a shallow basement of Archaean rocks and in a bedrock depression that parallels the trend of a large Cambrian-age shear zone described by Wilson and others (2007b). The surface of the glacier is subject to a mean annual temperature variation of from approximately -20°C to $+5^\circ\text{C}$.

The sampling sites are in the areas where the flow pattern was analysed by Patrick and others (2003) and are adjacent to a rock oasis known as the Vestfold Hills (Fig. 1a). The samples were obtained inland from the grounding line. The glacier thickness in this region varies from 70 to 160 m and the bed topography is irregular. A sub-horizontal ice foliation is seen in ice cliffs that border the Vestfold Hills, defined by alternating lenses or discontinuous layers of bubble-rich and clear ice incorporating variable amounts of dirt (Fig. 2). Foliation layers are typically 5–200 mm thick and are sometimes deformed into open folds (Fig. 2) as the ice moves over basement highs. Individual layers can be followed for tens to hundreds of metres as trails of air bubbles or coloured dust that makes the banding structure easily discernible in most parts of the ablation zone. There are also mesoscopic isoclinal folds and intense flattening in both the layering and recognizable ice-filled fractures (e.g. description of CG 1.7 site in Table 1), suggesting that this is in part a composite foliation. Foliation is restricted here to its microstructural meaning, i.e. the average flattening plane of the grains, *XY*, or, in a section parallel to the plane of the deformation, the average elongation direction *X*. It is also highly likely that the foliation in Sørsdal Glacier is a



Fig. 2. A section through Sørsdal Glacier adjacent to the Vestfold Hills, viewed looking south, showing the layering and the development of open asymmetric folds that indicate differential displacement of the ice mass to the west. Person is scale.

combination of inherited inhomogeneities and ice modified by shear strain as discussed by Hooke and Hudleston (1978).

Six cores were obtained from two sites referred to as the Russian Fuel Depot (RFD) and Christensen Grid (CG) where the ice movement and fracture patterns were recorded by Patrick and others (2003). At these sites the foliation was parallel to the glacier surface, and descriptions of the notable features observed at these localities are summarized in Table 1. At the RFD site, surface features were obscured by snow to the south and extensive surface recrystallization in the north. At the CG site, surface features were largely obscured by snow; however, CG 9.7 is in an area of largely stagnant ice. Crevasses are infrequent where flow rates are less than $\sim 27 \text{ m a}^{-1}$, but increase markedly in number and size across shear zones and areas of faster-moving ice (e.g. south of ice-drilling sites CG 3.6 and at CG 1.7 where the

ice is fast-moving and highly crevassed). The sampling locations (Fig. 1b and c) for all ice cores were oriented so that they intersect the nearly horizontal foliation at right angles. In the summer months the surface of this glacier is exposed to sunlight and there is localized surface melting of any snow accumulation. Sampling was undertaken in areas away from where any surface melt streams existed. The topmost and moist ice cover was removed with an ice axe, and cores $\sim 65 \text{ mm}$ in diameter and 1 to $\sim 4 \text{ m}$ long were drilled perpendicular to the foliation using a Kovacs drill (<http://www.kovacsicedrillingequipment.com>). Cores were reoriented and fitted together in the field to establish the air-bubble elongation direction. The cores recovered are believed to have developed their characteristics through a combination of thermal and mechanical processes outside the study area, and these have contributed to the glacier's rheological behaviour.

The cores were stored and transported from Antarctica for thin-section analysis in Melbourne, Australia, using two different versions of a G50 fabric analyser (<http://www.russellheadinstruments.com>), an instrument that determines the orientation of *c*-axes of uniaxial crystals at each pixel in the field of view (Wilson and others, 2003, 2007a). Initial analyses of the ice cores (Figs 3–5) and preparation of the Achsenverteilungsanalyse (AVA; axial distribution analysis) maps were undertaken using a G50-white instrument described by Wilson and others (2009). Subsequent investigations (Figs 6 and 7) used the instrument (G50-RGB) described by Peternell and others (2009, 2010, 2011), as this had a higher-resolution charge-coupled device (CCD) camera (2.8 vs $50 \mu\text{m}$ per pixel), and a light source provided by 11 light-emitting diodes (LEDs). This included eight inclined white LEDs with the addition of vertically oriented monochromatic red, green and blue (RGB) LEDs, and a $\lambda/4$ retarder plate that was moved from the lower polarizer to sit adjacent to the upper polarizer. By combining information from the digital images acquired by these instruments it was

Table 1. Summary of ice-core field data

Ice-core No.	Coordinates and elevation (UTM GRS80, zone 42)	Depth m	Surface velocity, azimuth	Comment
RFD 1.1	400108E, 2382403N, 268 m	4.10	22 m a^{-1} , 245°	Moderately to heavily crevassed with lenticular and sigmoidal en echelon geometries indicating dextral shear sense. Crevasse width 0.1–2 m; length 2–30 m. Recent crevasses (Sn) strike 140° ; earlier crevasse traces strike 160 – 180° (Sn-1), 200° (Sn-2) and 220 – 240° (Sn-3), i.e. the older traces approximate the southwest velocity vector in this region.
RFD 4.1	399894E, 2383232N, 273 m	3.75	22 m a^{-1} , 220°	Hairline fractures strike 300° . Crevasse traces are sparse.
CG 1.7	406795E, 2384761N, 440 m	2.90	61 m a^{-1} , 246°	Heavily crevassed with lenticular and sigmoidal en echelon geometries that indicate dextral shear sense. Crevasse width 0.4–2 m. Complex crevasse trace geometries, some folded and transposed, and the oldest traces strike 250° , sub-parallel to the calculated velocity vector. These are offset and overprinted by younger structures that strike 140° .
CG 3.6	406716E, 2385177N, 439 m	1.80	32 m a^{-1} , 250°	Similar to CG 1.7. Key difference is that the widths of the active crevasses are $< 1 \text{ m}$. Crevasse trace geometries are planar.
CG 6.7	406165E, 2385560N, 429 m	5.00	11 m a^{-1} , 255°	Active crevasses and traces still prominent, but fewer, and trace geometries appears less complex than at CG 9.7 site.
CG 9.7	406170E, 2386700N, 438 m	4.00	4.2 m a^{-1} , 261°	This is near the Sørsdal ice-stream margin, i.e. the boundary between fast-moving ice to the south and slow-moving plateau ice to the north. Surface structures are restricted to hairline fractures.

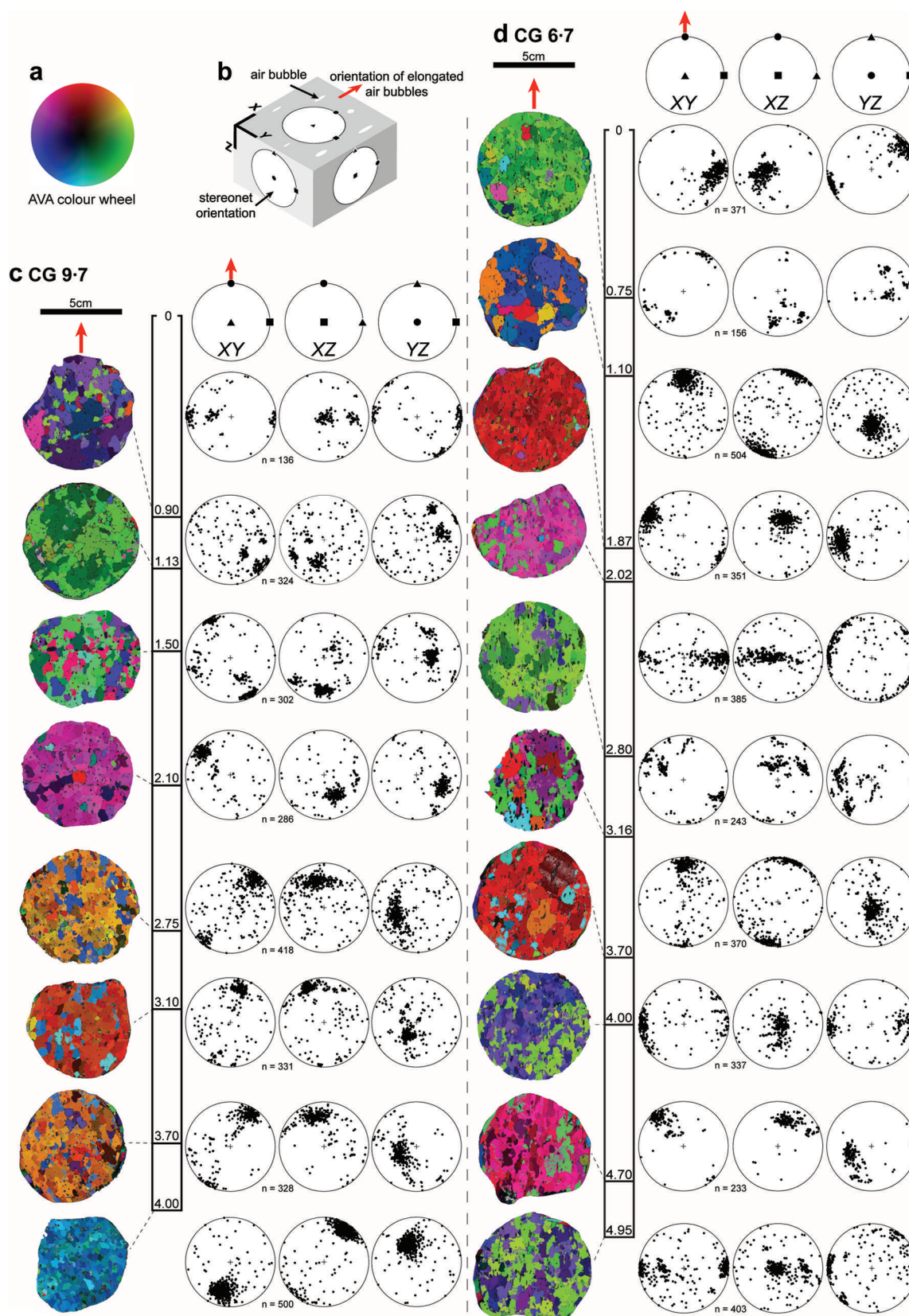


Fig. 3. The AVA orientations and *c*-axis fabric as a function of depth (m) in ice cores using the G50-white instrument. (a) The AVA colour code relates to the three-dimensional *c*-axis orientation, namely the azimuth and plunge of the *c*-axis at each pixel seen in the AVA map in an XY section. (b) Parameters used to illustrate the *c*-axes with reference to the air bubbles and local strain axes. (c) CG 9.7 (from the ice-stream margin) and (d) CG 6.7 (in area moving at 11 m a^{-1}). The grain microstructure in 65 mm diameter cores, on left of column, has the *c*-axis distribution, seen in a horizontal section, colour-labelled with respect to the AVA colour wheel. The direction of air-bubble alignment is indicated by red arrow. On right of column are the *c*-axis distributions in the three orthogonal sections adjacent to indicated core depths. The first column presents measurements from horizontal sections where the centre (triangle) coincides with the vertical core axis and the equator corresponds to the orientation of the foliation. The second and third columns represent the *c*-axis data rotated into the orthogonal vertical planes. All stereonet are equal-area lower-hemisphere projections; the number, *n*, of measured *c*-axes is shown at the bottom of the stereonet.

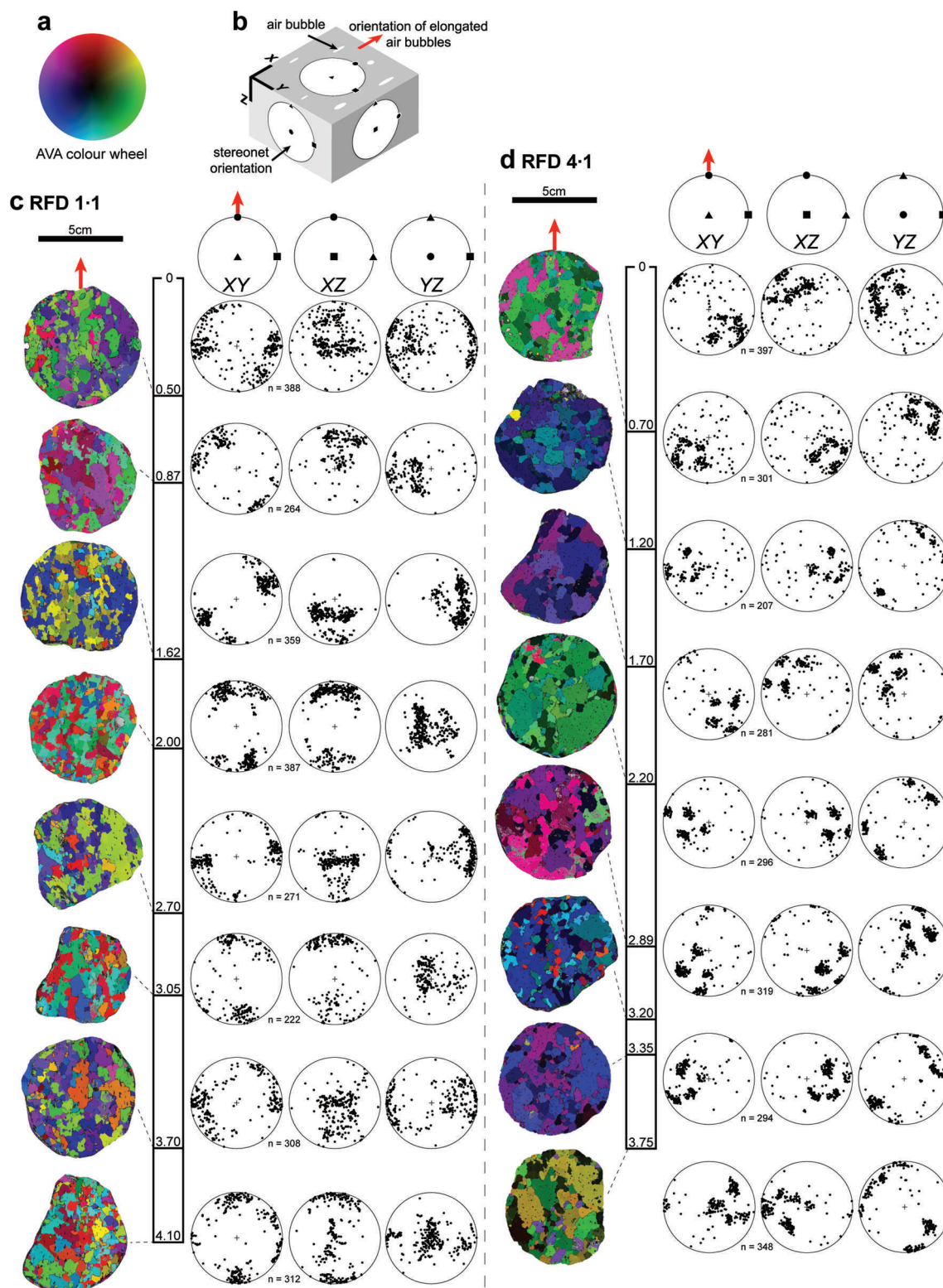


Fig. 4. The grain microstructure and AVA orientations with *c*-axis fabric as a function of depth (m) using the G50-white instrument in the 65 mm diameter cores. (a, b) As in Figure 3. (c) RFD 1.1 and (d) RFD 4.1, where the surface velocities are 22 m a^{-1} . The direction of air-bubble alignment is indicated by red arrow adjacent to AVA image.

possible to produce a composite dataset and AVA where gradational shades of colour represent variable *c*-axis orientations that can be attributed to each pixel in any field of view.

Colatitude (*c*-axis plunge from the vertical), retardation (highest birefringence colour), *c*-axis orientation trend, grain boundary and quality images are produced in addition to the

conventional crossed polar images. The data can be analysed individually using the G50 INVESTIGATOR software. From this the operator can obtain either a bulk crystallographic preferred orientation, or manually select, using a cursor, the trend and colatitude at any pixel site in an individual grain. Based on the quality of the data, doubtful results can be rejected (Peternell and others, 2009). This

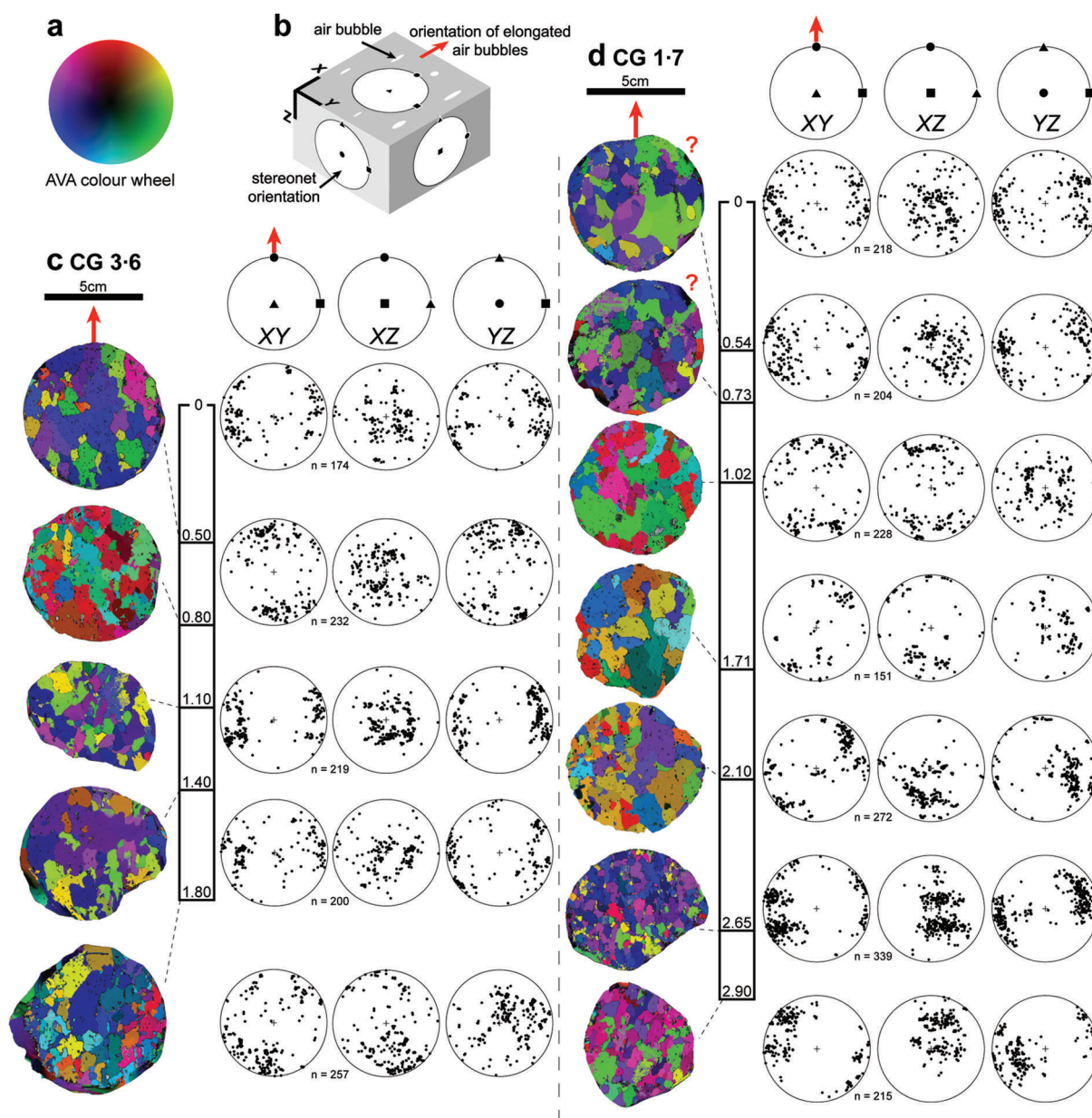


Fig. 5. The grain microstructure and AVA orientations with *c*-axis fabric as a function of depth (m) using the G50-white instrument in the 65 mm diameter cores. (a, b) As in Figure 3. (c) CG 3.6 (ice surface velocity 32 m a^{-1}). (d) CG 1.7 (ice surface velocity 61 m a^{-1}). The direction of air-bubble alignment is indicated by red arrow adjacent to AVA image, except at 0.54 and 0.73 m where there was no clear air-bubble alignment.

accounts for the different number of *c*-axes seen in the automatically generated crystallographic preferred orientation stereonets (Figs 3–7). Similarly if the crystal element being tested is not sufficiently uniform (due to minute impurities, grain boundaries, or air bubbles) it can immediately be identified, and a search can be made close to the selected site for clear crystal material.

Representative *c*-axis orientations from six cores are shown in Figures 3–5 as Schmidt lower-hemisphere equal-area stereographic projections. These *c*-axis plots are oriented so that the principal concentrations correspond to the colours that define the orientation quadrants indicated by the AVA colour wheel (Fig. 3a). Assuming that the rheological behaviour does not change significantly with ice depth, the *c*-axis framework in conjunction with the air-bubble alignment is used to establish domainal changes in the local transport within the near-surface ice mass. The

c-axes have been measured in the plane of flow, with confirmatory measurements obtained in vertical sections aligned parallel to air-bubble alignment (e.g. Fig. 6). The *c*-axis data have been rotated into three orthogonal principal strain trajectories that locally lie parallel to the *X*, *Y* and *Z* axes that are defined by the air-bubble alignment (Fig. 3b).

ICE MICROSTRUCTURAL CHARACTERISTICS

The six cores can be considered as representing five areas of increasing surface velocities within Sørsdal Glacier as observed from the strain marker estimations of Patrick and others (2003). The demarcation between these areas is not always clear, invariably because of the presence of crevasses (Table 1) that overprint the ductile deformation features observed in the ice, and there is no record of the nature of the earlier strain history preserved in the ice except

for occasional intrafolial folds and infilled and folded crevasses. With most cores, the initial mark for its orientation was lost between initiating drilling and fabric determination. A layering was visible in all cores and appeared to be defined by a varying density of air bubbles, but no folds were observed in the cores. Bubbles in the light layers are 1 mm in diameter and evenly distributed with ~ 5 mm between each bubble. The dark layers, which we attribute to a different light scattering, have noticeably fewer bubbles, which are randomly dispersed through the ice. However, the flow direction for the samples was estimated from the elongation of the air bubbles within the layering. These layers were grouped into three different classes based on air bubble density: (1) no bubbles, (2) low density ($< 2 \text{ cm}^{-2}$) and (3) medium density ($2\text{--}5 \text{ cm}^{-2}$). Ice grain sizes were measured directly from photographs taken from the G50 fabric analyser. These representative cores are described below.

CG 9.7 near the ice-stream margin

Horizontal thin sections were prepared at ~ 0.5 m intervals, parallel to the flow plane, to derive crystal-orientation fabric data combined with information on microstructures (Fig. 3c). In each section there were two grain populations: a general background of larger grains with diameters of 6–10 mm, within which were embedded smaller grains (~ 5 mm) with straight and slightly curved smooth grain boundaries. There is no obvious undulose extinction in any grains, and boundaries tend to be smoothly curved or straight.

In the first 1.5 m of core (Fig. 3c), which coincides with the greatest distribution of smaller grains and lack of air bubbles, there is a spread of c -axes and isolated concentrations. At 0.9 m (Fig. 3c) and 0.93 m (Fig. 6a) the c -axis orientations in the flow plane XY are dominated by crystals that lie perpendicular and at $\sim 45^\circ$ to the finite extension direction X defined by the air-bubble elongation. At 1.78 m (Fig. 6b) the majority ($\sim 80\%$) of c -axes lie close to the perpendicular to the bubble alignment that falls on a great circle plane. This plane is nearly parallel to the plane of cracks in the ice core shown as dashed lines on the stereonet in Figure 6a and b. Similar c -axis concentrations are observed (Fig. 3c) at 1.13 and 2.1 m, but rotated 45° to X within the flow plane XY .

From 2.75 to 4.0 m below the glacier surface, there was a marked elongation of air bubbles, but it did not coincide with any observable grain shape alignment (Fig. 3c). In the horizontal section XY , the air-bubble distribution was low and dominated by spherical bubbles with diameters of 0.2–1.0 mm that can be observed in the grain boundaries of the finer grain population. In the larger grains, there are more elongate grains with elongation ratios of > 10 that coexist with the spherical bubbles. There is a dominance of c -axis concentrations $10\text{--}30^\circ$ oblique to the direction of the grain elongation and air-bubble alignment (Fig. 3c).

Fine hairline cracks transect the grain microstructure occurring as either near-planar (Fig. 6a) or as an irregular surface that may contain small (> 2 mm) irregular ice grains (Fig. 6b). These structures have the appearance of a rough surface resembling stress-induced dissolution features that are comparable to what are known as stylolites in natural rocks (Ebner and others, 2009). However, in this case they are interpreted as dissolution and precipitation features produced by interfacial meltwater that has diffused along the planar cracks.

CG 6.7 area deforming at $\sim 11 \text{ m a}^{-1}$

This core has a medium density of elongate bubbles with elongation ratios that vary from spherical to > 15 (Fig. 3d). The microstructure in the first 1.1 m of the core is dominated by equant grains with individual concentrations of c -axes variably oriented with respect to the principal strain trajectory X . From 1.87 to 4.95 m the grains are more elongate interpenetrating crystals with no undulose extinction and a grain size of ~ 20 mm. This has been confirmed in vertical sections cut parallel to the air-bubble elongation.

The orientation patterns identified in the coloured AVA maps in CG 6.7 (Fig. 3d) show there are switches between the different RGB colour orientation groupings down the core, but fail to show any relationship between these orientation groups and their position in individual sections. These represent vertically stacked domains with distinct c -axis preferred orientation concentrations (Fig. 3d) that are dominated by strong single fabrics. These fabric concentrations are at a high angle to the bubble elongation direction (at 0.75, 2.8, 4.0 and 4.95 m), parallel (at 1.87 and 3.7 m) or oblique, i.e. $\sim 45^\circ$ to X (at 1.1, 2.02 and 4.7 m). This is comparable to the fabrics observed in the transition into the zones of greatest shear strain in the combined pure/simple shear experiments of Wilson and Sim (2002).

RFD 1.1 and RFD 4.1 areas deforming at $\sim 22 \text{ m a}^{-1}$

The microstructure in these two cores is characterized by interlocking grain structures with a grain size of ~ 20 mm and a lack of undulose extinction. An elongation direction defined by a low to medium air-bubble density existed throughout these cores, with a corresponding grain elongation that also defines the extension direction X . The ice in these cores showed the greatest variation in the c -axis fabrics, particularly with respect to the air-bubble alignment with the development of either double- or multiple-maxima c -axis fabrics.

In RFD 1-1 the ice at 0.5 and 0.87 m (Fig. 4c) shows a background scatter of orientations and two concentrations of c -axes at a high angle to the grain and air-bubble elongation X and lying on small-circle girdles oblique to the shortening axis Z . Between depths of 1.62 and 2.0 m these two concentrations of c -axes become asymmetric. From 2.7 to 4.1 m this basic pattern is retained with a minor distribution of c -axes in a small-circle girdle at a high angle to the air-bubble and grain elongation alignment. However, the air-bubble and grain shape alignment directions are changing along the core with respect to the c -axis patterns. The centre of the asymmetric small-circle girdle lies in the XY plane with opposed plunges of $\sim 45^\circ$, at 0.5 and 0.87 m, compared to the opposite plunge observed from 1.62 to 4.1 m.

In RFD 4.1 (Fig. 4d) a vertical change is obvious on the microscale by the contrasting switch in the AVA colours, namely the green (at 0.7, 2.2 and 3.75 m) versus the blue (at 1.2, 1.7, 2.89 and 3.35 m). In each horizontal thin section XY , there were scattered c -axis orientations, predominantly of the smaller grains, with four variably oriented c -axis concentrations, that define small-circle girdles, from the majority of the larger grains. There are 180° switches in these small-circle patterns down the core that can be correlated with visual changes on the surface of the core, namely the layering. This therefore represents domainal changes in c -axis orientation between layers in the ice core,

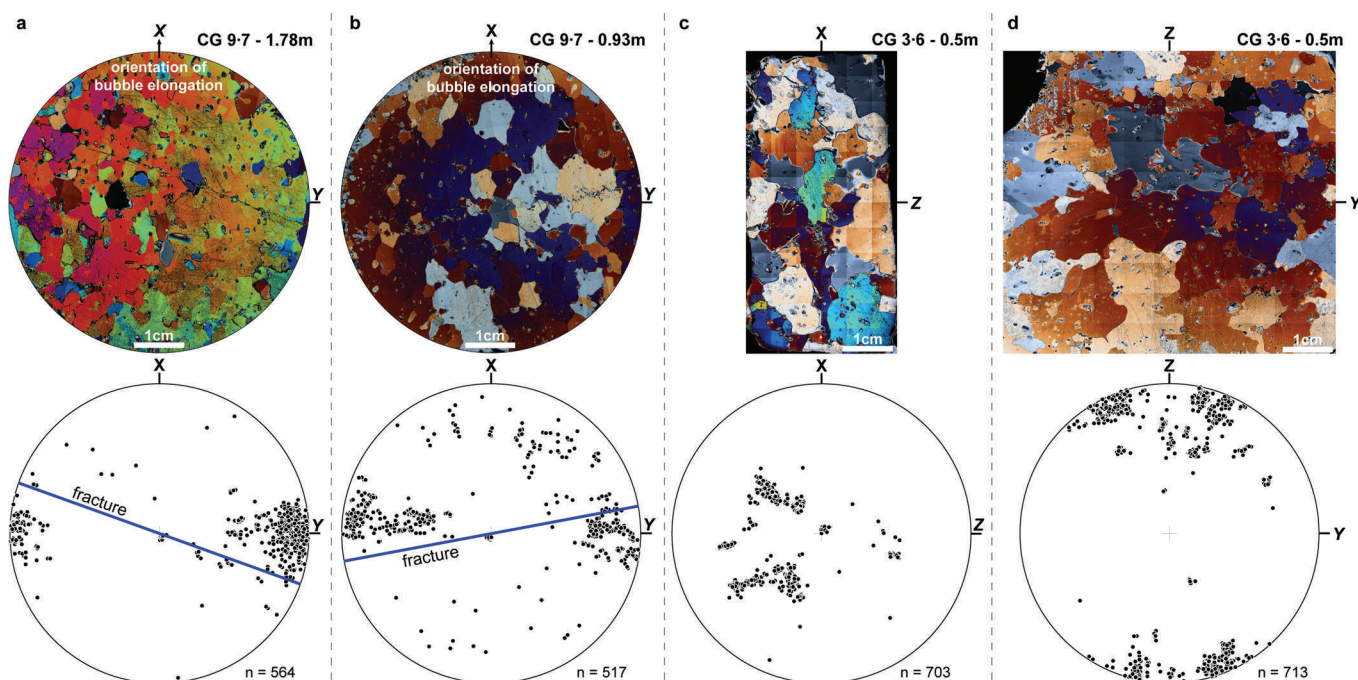


Fig. 6. Representative ice microstructures seen in retardation images (highest birefringence colours) with accompanying *c*-axis fabrics. (a) Horizontal XY section at 1.78 m in CG 9.7 with air-bubble alignment, X, and transacted by a near-planar fracture. (b) Horizontal section at 0.93 m in CG 9.7 transacted by an irregular fracture. (c) Vertical XZ section at 0.5 m in CG 3.6, perpendicular to the bubble elongation. The vertical and horizontal colour change in (c) and (d) represents a mismatch in retardation colour between adjacent tiles.

which has a strongly banded structure. The width of individual layers varies between 5 and 100 mm.

In RFD 4.1 (Fig. 4d), there are four maxima patterns that define the small-circle girdle, and unlike RFD 1.1 (Fig. 4c) there is little asymmetry in the *c*-axis patterns. The axis of the small-circle cones lies oblique to the inferred X and Z directions. These *c*-axis patterns resemble those described in the pure shear experiments of Wilson and Russell-Head (1982), where the maxima lie between 25° and 45° small-circle cones about the shortening axis Z. However, unlike the pure shear experiments, in this Sørsdal ice, the centre of the cones is offset from the inferred bulk strain axis Z, suggesting there is a rotational component to the simple shear. In fact these patterns are comparable to the *c*-axis patterns recognized in simple shear experiments (e.g. Bouchez and Duval, 1982; Burg and others, 1986).

CG 3.6 area deforming at $\sim 32 \text{ m a}^{-1}$

In horizontal XY sections this ice is typified by highly interlocked and slightly elongate grains (ratio of 1:3) with smoothly curved boundaries and sizes between 5 and 12 mm (though commonly ~ 7 mm). There is a low density of spherical and elongate air bubbles, with most contained in the grain boundaries. In vertical sections (Fig. 6c and d) the grains appear to overgrow the air bubbles with an elongation of the grains parallel to X (Fig. 6c) and parallel to Z (Fig. 6d).

The fabrics in this core (Fig. 5c) show a clustering of the *c*-axes as isolated concentrations that lie in diffuse small-circle girdles. The central axis of the small circle lies in the XY plane either at a high angle ($\sim 90^\circ$) to X (at 0.5, 1.1, 1.4 m) or obliquely (20–30°) to X (at 0.8, 1.8 m) and to the air-bubble alignment. In vertical sections, there are multi-maxima, off-axis small-circle distributions and this is clearly seen in sections parallel (Fig. 6c) and perpendicular (Fig. 6d)

to the elongation direction X. From the AVA colour maps, there is no indication of any spatial grouping of crystals with particular *c*-axis distributions.

CG 1.7 area deforming at $\sim 61 \text{ m a}^{-1}$

The ice in this area of higher surface velocities is coarser (Fig. 5d), with a highly interlocked grain structure and grains that tend to be elongate parallel to a bubble alignment in the horizontal section. Bubbles with elongation ratios of >10 dominate over spherical bubbles and define a clear elongation direction. There are coarser grains (~ 20 mm) at the top of the core (0.5–1.02 m), and a zone of smaller grains (5–10 mm) towards the base of the core (~ 2.65 –2.9 m). Coinciding with the coarsening at the top of the core, there is a lack of aligned air bubbles (e.g. at 0.54 and 0.73 m).

There is a progressive increase in *c*-axis fabric strength with depth, with all *c*-axes defining diffuse small-circle girdles, the axis of which lies within the XY plane. The spread of orientation concentrations may also reflect grain-size variations along the core; for instance at 1.7 m there are coarser grains with fewer *c*-axes compared to 2.65 m where there is an abundance of smaller grains. In CG 1.7 at 2.9 m (Fig. 5c), there is a noticeable bimodal distribution of *c*-axes. The variations in the AVA colours do not show the existence of any deformation domains or spatial distribution of the *c*-axes in the individual thin sections.

Evaluation of the accuracy of the *c*-axis fabrics

The fabric analyser G50-RGB has been calibrated against thin sections of quartz crystals measured on a universal stage and using EBSD techniques (Wilson and others, 2007a; Peternell and others, 2010). In order to compare the accuracy of the two versions of the fabric analyser, the same points within an ice grain were measured with both

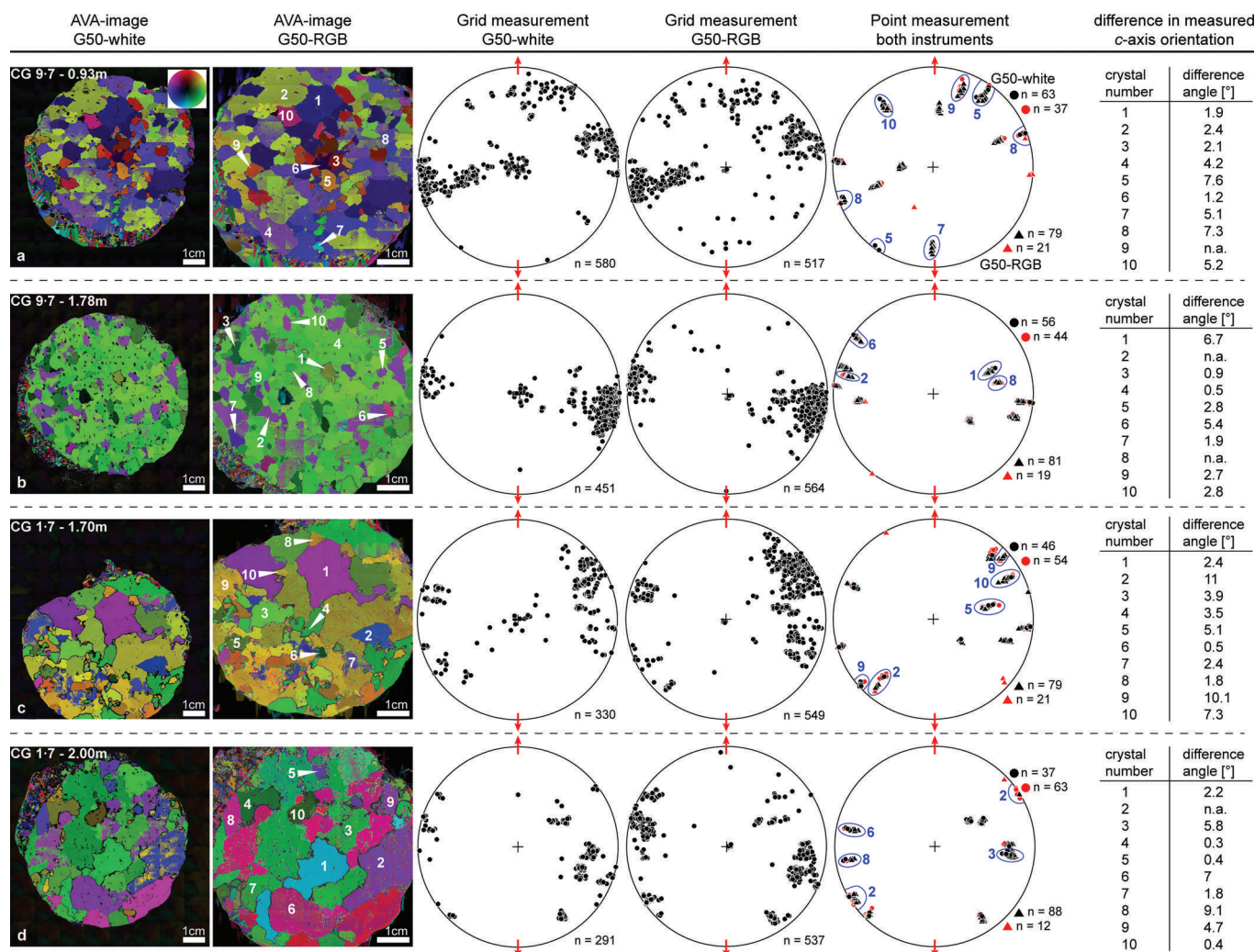


Fig. 7. Comparison of *c*-axis orientation measurements performed by two different versions of the fabric analyser (G50-white versus G50-RGB). (a–d) Results from ice-core samples CG 9.7(0.93 m), CG 9.7(1.78 m), CG 1.7(1.7 m) and CG 1.7(2.0 m). AVA images (columns 1 and 2) from the same horizontal ice thin section measured with the G50-white and G50-RGB instruments, respectively, with *c*-axis orientations colour-labelled with respect to the AVA colour wheel (a). Stereonets of bulk *c*-axis orientations (columns 3 and 4), where *n* is the number of measurements that passed the quality tests (Peternell and others 2009). Red arrows indicate elongation of air bubbles. The white arrowheads in column 2 mark crystals used for detailed comparison (columns 5 and 6). Within each crystal, ten measurements were performed and the results are presented in a lower-hemisphere, equal-area stereonet (column 5); circles are used for the G50-white, and triangles for the G50-RGB instrument; red symbols indicate measurements that failed the quality tests. Blue outlines and related numbers indicate the measurements within one crystal where differences in *c*-axis orientation between the two instruments are $>5^\circ$ (column 6). The *c*-axis orientation for one crystal is defined as the mean orientation of all single measurements (maximum ten) inside the crystal that passed the quality tests (black symbols in column 5). For some crystals none of the ten single measurements within one crystal passed the quality tests for the G50-white instrument, so the ‘difference angle’ is indicated as ‘n.a.’.

machines in four representative samples (Fig. 7). Both instruments use a CCD camera; the earlier G50-white instrument has a resolution of $50\ \mu\text{m}$ and the G50-RGB a resolution of $2.8\ \mu\text{m}$ per pixel. A total of 1000 measurements were made for each sample in a systematic grid pattern that can be attributed to each pixel in the field of view. These measurements were then filtered by two quality values generated by the instrument (Peternell and others, 2009). The number of measurements that passed the quality test was generally higher from the G50-RGB instrument. However, there are significant numbers of *c*-axes with near-vertical orientations identified by the G50-white instrument (Fig. 7, column 3), and with horizontal orientations by the G50-RGB instrument (Fig. 7, column 4). Many of the near-vertical *c*-axis orientations recorded by the G50-white instrument correlate with grain boundaries and are

thus invalid determinations. It is suggested that the algorithm that analyses the quality values with the $50\ \mu\text{m}$ per pixel takes a mean orientation and cannot detect small azimuthal variations, whereas the higher-resolution G50-RGB can detect small misorientations adjacent to grain boundaries (Peternell and others, 2009).

To further evaluate the quality of these *c*-axis measurements, 500 measurements in a grid pattern were compared with 10 separate grain measurements in each sample (Table 2). The ten randomly selected measurements were spatially related to a specific position within an ice-grain aggregate to enable repeatable selection and comparison (Fig. 7, columns 2 and 5). Within each grain a further ten randomly chosen measurements were made and the results are presented on a stereonet (Fig. 7, column 5), where circles are used for the G50-white instrument, and triangles

for the G50-RGB instrument. The red symbols indicate measurements that failed the quality value tests (Peternell and others, 2009); such measurements occur because all measured points were randomly chosen. The difference in angle between the two mean *c*-axis orientations, determined from the valid measurements inside an individual crystal, was then compared between instruments (Fig. 7, column 6). In the case of some ice crystals analysed by the G50-white (Fig. 7, columns 1 and 6), none of the ten single measurements within a single grain passed the geometric and retardation quality tests, so the 'difference angle' is not applicable (n.a.). These results can be compared with the 500 grid measurements (Table 2) and it can be seen that with a larger number of measurements the 'difference angle' is very comparable to the randomly selected ten points.

Using these automated methods it is the *c*-axes in some crystals with low angular resolutions ($\sim 0\text{--}30^\circ$) where large *c*-axis misorientations in geometric quality occur between both instruments. In such grains (blue ellipses in Fig. 7, column 5 and 6), the difference in *c*-axis orientation between the two instruments is $>5^\circ$. The explanation for this is that the estimation error in the algorithm with the G50-white is not as accurate as the G50-RGB instrument which has three additional LEDs and a higher CCD resolution.

The transition of light rays from air to ice to air has no influence on the fabric analyser measurements; this has already been described in the case of apatite crystals (Peternell and others, 2009). Light reflections and refractions from individual LEDs along air-bubble boundaries, crystal inclusions and fractures may lead to changes of the *c*-axis colatitude and azimuth (Peternell and others 2009). Nevertheless, because of the high resolution of the G50-RGB instrument such areas can be determined and incorrect measurements can be avoided, as the algorithm for determining the extinction plane that contains the *c*-axis is based on eight oblique white-light LEDs and the additional three vertical light directions of the near-monochromatic LEDs. In the case of the G50-RGB instrument, the extinction plane generated from the three vertical monochromatic light sources establishes the azimuth, and the *c*-axis colatitude is then determined from the mean of the intersection of the two outermost oblique planes with the plane from the vertical light source (Peternell and others, 2009).

DISCUSSION

From our observations the dominant rheological process that drives the deformation and recrystallization in Sørsdal Glacier is localization of ductile deformation parallel to the horizontal ice foliation, which pre-dates or is contemporaneous with the initiation of the brittle features responsible for the crevasse formation and current surface velocities. There were no significant microstructural differences from the areas dominated by stagnant ice (CG 9.7) versus the faster-moving portion of the glacier (CG 1.7); they are all dominated by large grains (5–20 mm) that overprint the foliation defined by an air-bubble alignment. The possibility that the higher surface velocities could account for a local coarsening of the grains is not supported by this study. As in other studies (e.g. Hooke and others, 1992), the greatest percentage of the surface velocity is probably due to sliding and deformation within the basal layer of ice and is

manifest at the surface as brittle deformation features. Nor are there significant changes in grain size suggesting seasonal temperature gradients might have driven rapid crystal growth in this near-surface ice, except in the top 1 m of CG 1.7 (Fig. 5d) where there are coarser grains and a lack of air-bubble alignment.

There were evident differences in the *c*-axis patterns in the areas of differing surface velocities, namely single maxima in CG 9.7 and CG 6.7 (Fig. 3c and d), an asymmetric bimodal small circle in RFD 1.1 (Fig. 4c), an oblique four-maxima small circle in RFD 4.1 (Fig. 4d) and diffuse small-circle girdles with bimodal or multi-maxima concentrations in the faster-moving ice in CG 3.6 and CG 1.7 (Figs 5c and d and 6c and d). All these patterns might be explained by deformation in a simple shear regime, dominated by slip on the soft basal plane. These observations are similar to the results described in experimentally deformed ice (e.g. Kamb, 1972; Bouchez and Duval, 1982; Burg and others, 1986; Wilson and Sim, 2002). In these simple shear experiments, the crystals develop an elongate shape and a new *c*-axis fabric that, at small strains, develops two distinct orientations and evolves into a broad single asymmetric fabric at higher strains symmetrically related to the foliation or plane of flattening, *XY*.

In Sørsdal Glacier ice, there is discordance in the azimuthal concentrations of *c*-axes along the length of a core, and these probably represent local rotations in the foliation plane *XY* with respect to the bulk strain axes. These major variations in *c*-axis patterns with respect to the air-bubble elongation are summarized in Figure 8. There is a marked switch in *c*-axis patterns in individual cores, from small circles containing double maxima (Fig. 8a) to oblique single-maxima concentrations (Fig. 8b), back to asymmetric double maxima (Fig. 8c) and off-centre small circle concentrations that may be symmetric or asymmetric distributions of *c*-axes (Fig. 8d).

In all the *c*-axis fabric diagrams (Figs 3–5), except for GC 6.7(4 m, 4.95 m), RFD 1.1(4.10 m) and CG 3.6(1.1 m), the local *c*-axes do not coincide with the local strain axes *XYZ* identified from the air-bubble elongation and cannot be reconciled with the directions of flow observed in the surface velocity data (Fig. 1b and c; Patrick and others, 2003). As such, the deformation path of any individual point in the ice mass can be considered as non-coaxial and spatially unique, particularly in its domainal or cyclic variation down a core. Where there has been a coaxial deformation, a steady-state *c*-axis preferred orientation will develop (Wilson and Russell-Head, 1982) and the deviation from this during a non-coaxial deformation is contingent on whether the grains have retained the orientation of earlier elements (e.g. foliation) or whether the orientation is being continuously modified by intracrystalline slip. The microstructure can be continuously modified, but, as described by Wilson (1981), there may be a lag in modifying the previous *c*-axis preferred orientation as different intracrystalline slip mechanisms are brought into action.

The *c*-axis fabrics are also comparable to fabrics obtained from deeper Antarctic ice cores (Gow, 1963; Thwaites and others, 1984) where a small component of simple shear superimposed on uniaxial compression produces domainal fabric patterns with alternations of layers with *c*-axes concentrated as maxima and/or small-circle girdles perpendicular to the foliation. As argued by Dahl-Jensen and others (1997), such fabrics can be assumed to develop under

Table 2. Comparison of *c*-axis orientation measurements performed by two different versions of the fabric analyser (G50-white versus G50-RGB) using 500 grid versus 10 random points in ice-core samples CG 9.7(0.93 m), CG 9.7(1.78 m), CG 1.7(1.7 m) and CG 1.7(2.0 m)

Sample, crystal	G50-	Number of measurements		Mean orientation		Misorientation statistic crystal – mean orientation			Difference angle G50-RGB/white	
		Total	rg, gq* >75	Azimuth	Plunge	Min./max.	Mean	Std dev.	~500 points (grid selection)	10 points (random selection, Fig. 7)
CG 9.7(0.93 m)										
1	RGB	489	480	252	38.50	0.04/9.94	1.98	1.49	3.51	1.9
	White	500	216	252	42.01	0.17/4.21	1.43	0.83		
2	RGB	490	482	67.24	30.11	0.01/6.85	1.82	1.39	3.53	2.4
	White	500	342	67.65	26.60	0.04/5.07	1.54	1.02		
3	RGB	489	486	6.39	41.42	0.03/9.38	2.30	1.67	2.32	2.1
	White	500	482	5.88	39.13	0.03/4.72	0.79	0.64		
4	RGB	490	381	274.14	8.26	0.05/9.27	1.77	1.37	4.04	4.2
	White	496	376	274.11	4.22	0.17/6.31	1.81	1.22		
5	RGB	501	407	36.33	13.73	0.07/10.59	2.73	1.95	6.12	7.6
	White	491	278	36.14	7.61	0.20/15.36	2.71	2.15		
6	RGB	501	501	275.54	65.46	0.03/4.25	0.92	0.63	1.48	1.2
	White	491	487	272.01	65.67	0.02/2.74	0.68	0.39		
7	RGB	489	482	180.41	25.66	0.01/5.96	1.50	1.14	2.49	5.1
	White	501	400	180	23.20	0.07/6.50	1.47	1.06		
8	RGB	500	211	249.29	6.95	0.24/12.33	2.99	2.3	1.37	7.3
	White	489	145	247.96	7.30	0.03/5.29	1.60	1.1		
9	RGB	491	379	20.52	19.34	0.05/12.00	3.70	2.67	1.56	n.a.
	White	489	86	20.13	17.82	0.06/9.22	2.27	1.95		
10	RGB	500	488	322	29.15	0.06/7.44	2.11	1.46	7.80	5.2
	White	490	473	322.17	21.35	0.18/8.80	2.15	1.4		
CG 9.7(1.78 m)										
1	RGB	496	480	68.01	39.58	0.05/7.59	1.7	496	4.53	6.7
	White	496	315	67.31	35.08	0.08/3.72	1.03	496		
2	RGB	501	501	282.51	12.74	0.03/6.42	1.39	501	2.45	n.a.
	White	490	9	281.64	10.44	0.73/4.56	2.08	490		
3	RGB	500	500	125.83	52.96	0.01/3.54	0.8	500	0.54	0.9
	White	496	483	126.47	52.59	0.12/3.20	1.16	496		
4	RGB	500	451	94.72	13.43	0.05/4.83	1.15	500	1.09	0.5
	White	500	193	95.11	14.45	0.06/3.59	0.96	500		
5	RGB	489	364	275.25	2.91	0.05/5.50	1.19	489	18.18	2.8
	White	496	192	95.35	15.27	8.08/15.27	11.84	496		
6	RGB	490	380	306.5	6.98	0.12/6.49	1.74	490	3.42	5.4
	White	500	449	304.5	4.2	0.04/5.29	1.15	500		
7	RGB	489	403	265.11	26.8	0.07/12.63	2.33	489	2.11	1.9
	White	490	478	262.96	27.69	0.02/3.44	0.8	490		
8	RGB	496	495	114.94	21.76	0.06/8.05	1.81	496	33.63	n.a.
	White	500	16	79.47	34.82	0.09/3.83	0.93	500		
9	RGB	496	495	104.4	15.3	0.03/4.65	1.05	496	2.71	2.7
	White	500	486	106.4	17.21	0.02/4.13	1.1	500		
10	RGB	496	480	287.37	8.74	0.10/8.02	2.22	496	2.67	2.8
	White	500	447	286.92	6.11	0.06/8.78	1.61	500		
CG 1.7(1.70 m)										
1	RGB	489	430	292.9	14.58	0.06/13.05	3.18	2.33	2.13	2.4
	White	490	328	292.08	16.56	0.01/7.35	1.61	1.16		
2	RGB	492	447	221	11.87	0.04/12.42	3.23	2.35	11.86	11
	White	490	23	220.35	23.71	0.05/5.32	1.81	1.3		
3	RGB	496	496	95.67	9.41	0.01/5.87	1.32	1.02	2.71	3.9
	White	491	391	95.15	6.75	0.06/5.90	1.47	1.11		
4	RGB	489	483	105.88	25.85	0.01/4.04	1.09	0.81	2.46	3.5
	White	501	269	106.02	23.39	0.02/4.99	0.77	0.68		
5	RGB	489	489	78.44	44.02	0.03/3.47	0.83	0.6	3.68	5.1
	White	490	97	77.14	40.47	0.14/7.17	1.88	1.37		
6	RGB	496	496	125.99	61.27	0.03/2.93	0.77	0.51	0.18	0.5
	White	490	482	125.87	61.44	0.01/1.34	0.29	0.21		
7	RGB	492	331	253.55	5.31	0.13/11.73	3.87	2.45	0.38	2.4
	White	489	431	253.8	5.6	0.03/5.50	1.18	0.87		
8	RGB	500	459	42.75	18.12	0.07/10.55	2.96	2.2	5.68	1.8
	White	492	48	42.25	12.46	0.33/12.90	3.26	2.83		
9	RGB	500	499	47.99	8.25	0.03/8.75	1.84	1.36	14.33	10.1
	White	500	270	227.62	6.08	0.31/11.39	5.02	2.41		
10	RGB	500	483	61.35	19.17	0.04/11.50	2.16	1.66	5.74	7.3
	White	500	30	61.46	13.43	0.44/5.97	1.73	1.26		

Table 2. continued

Sample, crystal	G50-	Number of measurements		Mean orientation		Misorientation statistic crystal – mean orientation			Difference angle G50-RGB/white	
		Total	rg, gq* >75	Azimuth	Plunge	Min./max.	Mean	Std dev.	~500 points (grid selection)	10 points (random selection, Fig. 7)
CG 1.7(2.00 m)										
1	RGB	492	440	146.47	15.81	0.04/3.76	0.85	0.63	0.82	2.2
	White	500	97	146.94	16.5	0.20/5.01	1.44	0.96		
2	RGB	489	470	234.69	5.12	0.02/4.97	1.24	0.94	0.40	n.a.
	White	500	14	234.4	5.39	0.73/9.92	4.21	2.43		
3	RGB	489	369	95.28	22	0.05/6.59	1.86	1.28	6.08	5.8
	White	489	315	95.8	28.06	0.01/6.94	1.71	1.13		
4	RGB	489	489	62.35	45.31	0.02/2.99	0.76	0.54	0.47	0.3
	White	500	109	61.69	45.41	0.01/5.22	1.26	0.84		
5	RGB	489	479	224.36	5.75	0.04/4.96	1.38	0.94	2.86	0.4
	White	501	357	224.42	2.89	0.03/5.80	1.08	0.83		
6	RGB	490	467	282.24	19.46	0.14/13.82	3.15	2.36	6.42	7.0
	White	496	343	281.5	13.08	0.03/4.00	1.11	0.77		
7	RGB	501	486	88.17	22.8	0.01/4.59	1.01	0.75	6.67	1.8
	White	500	9	87.73	29.46	0.2/2.32	0.95	0.92		
8	RGB	500	476	261.76	16.89	0.01/3.42	0.78	0.56	7.72	9.1
	White	489	19	261.09	9.2	0.10/6.37	1.73	1.72		
9	RGB	489	487	238.64	6.28	0.02/5.41	1.37	1.01	1.70	4.7
	White	490	317	238.65	4.58	0.10/9.78	3.47	2.04		
10	RGB	489	483	52.31	54.19	0.01/3.49	0.94	0.58	1.13	0.4
	White	490	355	53.2	55.2	0.02/3.80	0.53	0.38		

*rq (retardation quality) and gq (geometric quality) are values to evaluate the quality of a fabric analyzer measurement; Both values range between 0 (measurement rejected) and 100 (excellent).

uniaxial unconfined compression (parallel to Z) as most of these drill sites are located close to the summit of ice domes. In the case of Sørsdal Glacier ice described here, most of the fabrics are oblique or at a high angle to Z and are more akin to the fabric transition into a sheared ice mass (Hudleston, 1977) and hence are not representative of strain conditions in their current location (Hooke and Hudleston, 1978). The multi-maxima and grains with c -axes concentrating in the flow plane at a low angle to the flow direction (Fig. 4) and their cyclic or domainal distribution patterns also resemble the fabrics recognized by Thwaites and others (1984) in zones of high closure in drill holes that were attributed to naturally occurring shear zones.

In general, the grain alignment observed in most thin sections might be explained by anisotropic growth with dependence for the grain boundary mobility on crystallographic orientation. However, this mechanism is unlikely to be important in this particular case because the preferred orientation of ice grains does not correspond well with the foliation and air-bubble alignment. The dominant layering or banding on the surface of the cores probably reflects domains with obliquely aligned c -axis concentrations with respect to the locally constant air or grain alignment in any particular core. This probably arises from a localization of differential strains in a horizontal plane, with the strain axis Z normal to the foliation, and subsequent grain growth overprinting the pre-existing foliation. However, it is possible that in the course of continuous deformation the strain axes Y and Z may have been switching based on observations of deformed crevasses in the fastest-flowing zones (e.g. CG1.7 in Table 1). Therefore a dominant component of any vertically

oriented compressive stress in developing the ice micro-fabric cannot be estimated. This suggests that the prevailing fabric in the ice investigated here was developed upstream in Sørsdal Glacier in areas of higher shear stress without significant microstructural modification, except for the superimposed brittle deformation.

It has been shown that although distinct fabric patterns exist, there is only limited evidence of later deformation in the form of undulose extinction, and this we attribute to the later brittle deformation. This does not appear to influence the evolution of the fabric pattern, as dynamic recrystallization of more favourably oriented grains, by selective migration recrystallization, probably accommodates local stress changes. There also appeared to be a good correlation between grain shape and size, with more elongation with increasing bubble density. This was most evident where there was a strong orientation pattern, particularly where there was a clustering of grains together with a like orientation pattern.

The role of an interfacial liquid phase on the development of these orientation patterns could not be ascertained. A liquid phase diffusing from any surface melting could contribute to the accommodation of intracrystalline slip; however, this is unlikely as there is a lack of undulose extinction in the ice grains to support such deformation. As suggested by Lliboutry (1996), the effect of water in promoting some grain adjustment is also ruled out as there are no structures that would support evidence for interstitial water. Instead percolation of meltwater appears to have been along fractures which now resemble stress-induced dissolution features that are comparable to what are known as stylolites in natural rocks (Ebner and others, 2009).

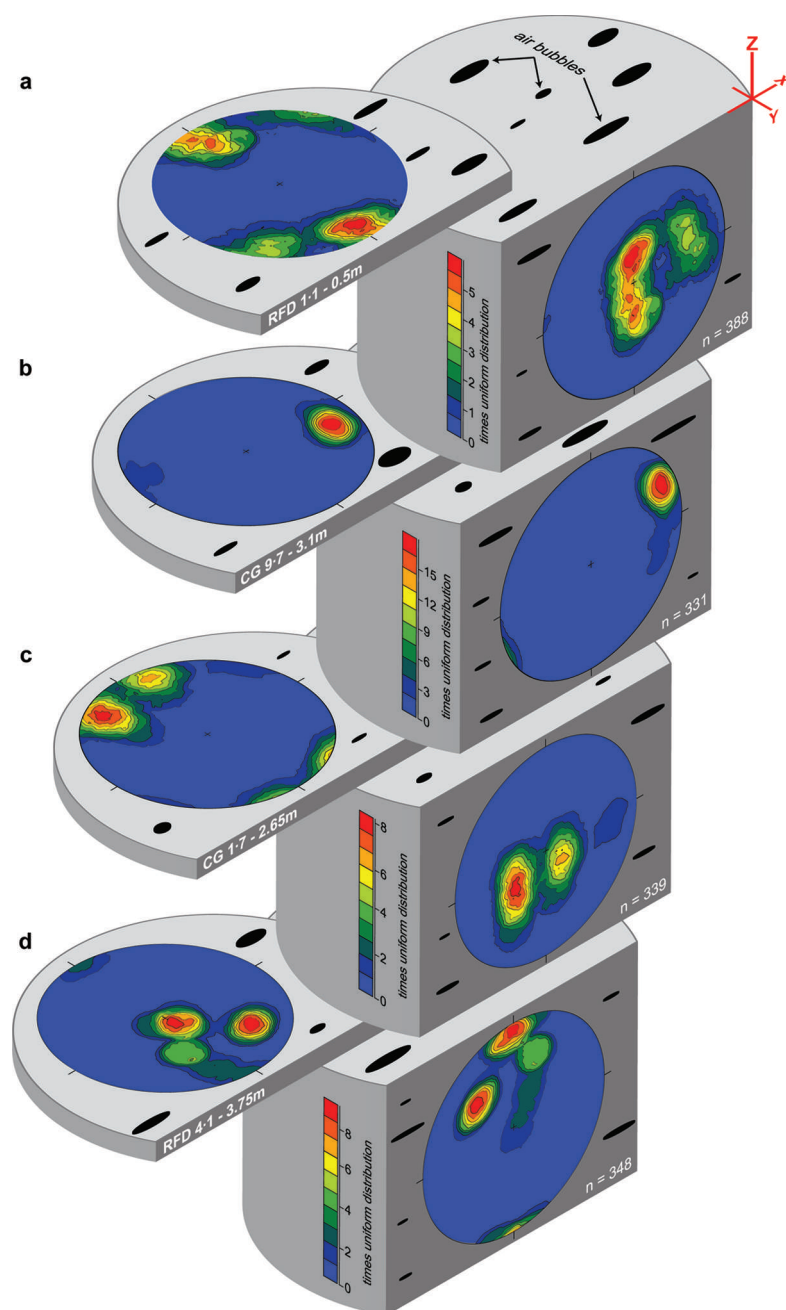


Fig. 8. Summary of *c*-axis variations observed in horizontal XY and corresponding vertical XZ section in relationship to the air-bubble alignment in the ice from Sørsdal Glacier. The contoured fabric diagrams are based on representative stereonet from Figures 3–5, and the contour intervals are multiples of a uniform distribution.

CONCLUSIONS

The surface velocity of Sørsdal Glacier has little to do with the evolution of the microstructure and *c*-axis patterns recognized in the bulk of its surface ice mass. The ice is highly anisotropic, with a prominent grain elongation and air-bubble alignment that is accompanied by a *c*-axis fabric that developed in a simple shear regime without any major microstructural changes that can be attributed to its local stress environment. This ice has probably been brought to the surface as a result of large-scale irregularities in the bed topography. In such an area the surface velocities and brittle deformation could be the principal manifestation of this influence. This brittle deformation has not significantly modified the inherited microfabric which evolved earlier in its transport history and not in its current location.

The application of the higher-resolution G50-RGB as described in this study represents an important step in analysing ice crystal fabrics. Using the AVA maps, rapid changes in fabrics can easily be detected in any vertically oriented ice core. However, high-accuracy measurements depend on the spatial resolution of the CCD camera, and the accuracy can be improved by the incorporation of additional RGB LEDs into the illumination system.

ACKNOWLEDGEMENTS

We thank A. Corvino and B. Patrick for collecting the ice cores during their investigations of Sørsdal Glacier, and H. Sim for his initial microfabric results. This work was supported by an Australian Research Council grant

(DP0773097), an Antarctic Science Advisory Committee grant (1205) and the ANARE expeditioners (Australian National Antarctic Research Expeditions) of Davis Station from 2000 to 2003. D. Russell-Head is thanked for technical advice and assistance, including the redesign and modifications of the G50 instrument, and comments on the manuscript. J.-L. Tison (Université de Bruxelles) is thanked for making available his G50 (LED-white) that enabled us to undertake the comparative test. A. Corvino, S. Kipfstuhl and two anonymous reviewers are thanked for constructive feedback on an earlier version of the paper.

REFERENCES

- Bouchez, J.L. and P. Duval. 1982. The fabric of polycrystalline ice deformed in simple shear: experiments in torsion, natural deformation and geometrical interpretation. *Textures Microstruct.*, **5**(3), 171–190.
- Burg, J.P., C.J.L. Wilson and J.C. Mitchell. 1986. Dynamic recrystallisation and foliation development during the simple shear deformation of ice. *J. Struct. Geol.*, **8**(8), 857–870.
- Dahl-Jensen, D., T. Thorsteinsson, R. Alley and H. Shoji. 1997. Flow properties of the ice from the Greenland Ice Core Project ice core: the reason for folds? *J. Geophys. Res.*, **102**(C12), 26,831–26,840.
- Ebner, M., D. Koehn, R. Toussaint, F. Renard and J. Schmittbuhl. 2009. Stress sensitivity of stylonite morphology. *Earth Planet. Sci. Lett.*, **277**(3–4), 394–398.
- Goldsby, D.L. 2009. Superplastic flow of ice relevant to glacier and ice-sheet mechanics. In Knight, P.G., ed. *Glacier science and environmental change*. Oxford, Wiley-Blackwell, 308–314.
- Gow, A.J. 1963. Results of measurements in the 309 meter bore hole at Byrd Station, Antarctica. *J. Glaciol.*, **4**(36), 771–784.
- Hooke, R.LeB. and P.J. Hudleston. 1978. Origin of foliation in glaciers. *J. Glaciol.*, **20**(83), 285–299.
- Hooke, R.LeB., V.A. Pohjola, P. Jansson and J. Kohler. 1992. Intra-seasonal changes in deformation profiles revealed by borehole studies, Storglaciären, Sweden. *J. Glaciol.*, **38**(130), 348–358.
- Hudleston, P.J. 1977. Progressive deformation and development of fabric across zones of shear in glacial ice. In Saxena, S. and S. Bhattacharji, eds. *Energetics of geological processes*. Amsterdam, Springer Verlag, 121–150.
- Kamb, B. 1972. Experimental recrystallization of ice under stress. In Heard, H.C., I.Y. Borg, N.L. Carter and C.B. Raleigh, eds. *Flow and fracture of rocks*. Washington, DC, American Geophysical Union, 211–241. (Geophysical Monograph 16.)
- Lliboutry, L. 1996. Temperate ice permeability, stability of water veins and percolation of internal meltwater. *J. Glaciol.*, **42**(141), 201–211.
- Patrick, B.A., A.F. Corvino and C.J.L. Wilson. 2003. Ice-flow measurements and deformation at marginal shear zones on Sørsdal Glacier, Ingrid Christensen Coast, East Antarctica. *Ann. Glaciol.*, **37**, 60–68.
- Peternell, M., F. Kohlmann, C.J.L. Wilson, C. Seiler and A.J.W. Gleadow. 2009. A new approach to crystallographic orientation measurement for apatite fission track analysis: effects of crystal morphology and implications for automation. *Chemical Geol.*, **265**(3–4), 527–539.
- Peternell, M., P. Hasalova, C.J.L. Wilson, S. Piazzolo and K. Schulmann. 2010. Evaluating quartz crystallographic preferred orientations and the role of deformation partitioning using EBSD and fabric analyser techniques. *J. Struct. Geol.*, **32**(6), 803–817.
- Peternell, M., D.S. Russell-Head and C.J.L. Wilson. 2011. A technique for recording polycrystalline structure and orientation during in situ deformation cycles of rock analogues using an automated fabric analyser. *J. Microsc.*, **242**(2), 181–188.
- Petrenko, V.F. and R.W. Whitworth. 1999. *Physics of ice*. Oxford, etc., Oxford University Press.
- Poirier, J.P. 1980. Shear localization and shear instability in materials in the ductile field. *J. Struct. Geol.*, **2**(1–2), 135–142.
- Thorsteinsson, T., J. Kipfstuhl and H. Miller. 1997. Textures and fabrics in the GRIP ice core. *J. Geophys. Res.*, **102**(C12), 26,583–26,599.
- Thwaites, R.J., C.J.L. Wilson and A.P. McCray. 1984. Relationship between bore-hole closure and crystal fabrics in Antarctic ice core from Cape Folger. *J. Glaciol.*, **30**(105), 171–179.
- Wilen, L.A., C.L. DiPrinzio, R.B. Alley and N. Azuma. 2003. Development, principles, and applications of automated ice fabric analyzers. *Microsc. Res. Techn.*, **62**(1), 2–18.
- Wilson, C.J.L. 1981. Experimental folding and fabric development in multilayered ice. *Tectonophysics*, **78**(1–4), 139–159.
- Wilson, C.J.L. 2000. Experimental work on the effect of pre-existing anisotropy on fabric development in glaciers. In Maltman, A.J., B. Hubbard and M.J. Hambrey, eds. *Deformation of glacial materials*. London, Geological Society, 97–113. (Special Publication 176.)
- Wilson, C.J.L. and D.S. Russell-Head. 1982. Steady-state preferred orientation of ice deformed in plane strain at -1°C . *J. Glaciol.*, **28**(98), 145–160.
- Wilson, C.J.L. and H.M. Sim. 2002. The localization of strain and c-axis evolution in anisotropic ice. *J. Glaciol.*, **48**(163), 601–610.
- Wilson, C.J.L., D.S. Russell-Head and H.M. Sim. 2003. The application of an automated fabric analyzer system to the textural evolution of folded ice layers in shear zones. *Ann. Glaciol.*, **37**, 7–17.
- Wilson, C.J.L., D.S. Russell-Head, K. Kunzi and G. Viola. 2007a. The analysis of quartz c-axis fabrics using a modified optical microscope. *J. Microsc.*, **227**(1), 30–41.
- Wilson, C.J.L., C. Quinn, L. Tong and D. Phillips. 2007b. Early Palaeozoic intracratonic shears and post-tectonic cooling in the Rauer Group, Prydz Bay, East Antarctica constrained by $40\text{Ar}/39\text{Ar}$ thermochronology. *Antarct. Sci.*, **19**(3), 339–353.
- Wilson, C.J.L., J.A. Robinson and A.L. Dugdale. 2009. Quartz vein fabrics coupled to elevated fluid pressures in the Stawell gold deposit, south-eastern Australia. *Mineral. Depos.*, **44**(3), 245–263

MS received 1 December 2010 and accepted in revised form 16 July 2011